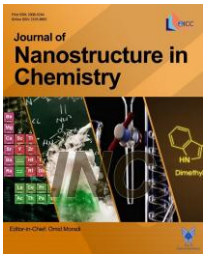

J. Nanostruct Chem. 2026; 16(1): 1-19

Journal of Nanostructure in Chemistry (JNSC)

https://doi.org/10.57647/jnsc.2026.1601.01

Research Article

Silver Nanoparticle–Decorated PCL Scaffolds: In-Vitro Antimicrobial Activity and Effects on Osteogenic Cell Responses

Xiaogang Zhou[#], An'nan Hu[#], Jian Zhou[#,*]

Department of Orthopaedic Surgery, Zhongshan Hospital, Fudan University, Shanghai 200032, China

[#]*These authors contributed equally to this work*

[*]**Corresponding authors:** Zhou.jian1@zs-hospital.sh.cn

Article History:

Received:
13 September 2025

Revised:
16 October 2025

Accepted:
02 November 2025

Published in Issue:
28 February 2026

Abstract

To engineer and evaluate silver nanoparticle–decorated polycaprolactone (PCL) scaffolds that simultaneously provide antibacterial activity and support osteogenic cell responses for bone tissue engineering. Methods: Electrospun PCL scaffolds were functionalized by in situ chemical reduction of $AgNO_3$ to generate uniformly distributed AgNPs and then characterized by TEM/XRD, EDS/XPS, FTIR/XRD, and porosity analyses. Antibacterial performance was tested against Staphylococcus aureus and Escherichia coli by disk diffusion and CFU assays, while MC3T3-E1 preosteoblast responses were assessed by CCK-8 proliferation, ALP activity, and osteogenic gene expression. Results: AgNPs averaged ~22 nm; surface silver content was ~3.2 at% (~0.8 wt%), yielding sustained Ag^+ release of ~0.4 µg per 50 mg scaffold over 21 days (~80% by day 14). PCL–Ag scaffolds produced inhibition zones of 12.5 ± 0.5 mm (S. aureus) and 11.0 ± 0.4 mm (E. coli) and achieved >99.9% bacterial reduction in suspension. MC3T3-E1 proliferation increased relative to PCL controls (day-7 OD450 2.50 ± 0.15 vs. 2.08 ± 0.12; $p<0.01$). Early osteogenesis was enhanced, with ALP 1.8× at day 7 and 1.5× at day 14, accompanied by upregulated RUNX2 and BMP2; scaffold porosity and PCL crystallinity were preserved. Conclusions: In situ AgNP decoration confers durable antibacterial activity while promoting osteogenic cell functions, indicating a promising infection-resistant platform for bone regeneration.

Keywords: Antibacterial efficacy; Biomaterial characterization, Nanofibrous scaffold; Osteogenic differentiation; Silver ion release

Cite this article: Zhou, X., Hu, A., Zhou, J. Silver Nanoparticle–Decorated PCL Scaffolds: In-Vitro Antimicrobial Activity and Effects on Osteogenic Cell Responses. *J Nanostruct Chem* **16**, 1-19 (2026). https://doi.org/1057647/jnsc.2026.1601.01

1. Introduction

Bone tissue engineering aims to develop scaffolds that not only support new bone growth but also prevent infection, which is a major complication in orthopedic implants [1]. Polycaprolactone (PCL) is a widely used biodegradable polymer for scaffolds due to its biocompatibility and mechanical flexibility, but it lacks intrinsic osteogenic and antimicrobial properties [2]. On the other hand, silver nanoparticles (AgNPs) are well-known for broad-spectrum antimicrobial activity against bacteria (including antibiotic-resistant strains) while exhibiting low toxicity to mammalian cells at appropriate doses [3]. Incorporating AgNPs into PCL scaffolds offers a promising strategy to create a multifunctional biomaterial that can prevent infection and support bone regeneration simultaneously.

Recent studies have shown that scaffolds enriched with silver can inhibit microbial growth and even promote osteoblastic differentiation of stem cells when the silver content is kept at non-cytotoxic levels [4]. AgNPs provide antimicrobial effects through multiple mechanisms, including release of Ag^+ ions that disrupt microbial membranes and proteins [5], and generation of reactive oxygen species [6]. By decorating PCL scaffolds with AgNPs, the scaffold surface can act as a reservoir for continuous silver ion release, achieving localized antibacterial action without systemic toxicity [7]. However, it is critical to control the silver loading and release rate, as excessive Ag^+ can be cytotoxic and impede tissue healing [8]. Thus, an optimal in situ synthesis of AgNPs within the scaffold can ensure effective bacterial killing while maintaining biocompatibility. Furthermore, incorporating AgNPs may modify scaffold surface properties – for example, improving hydrophilicity or roughness – which can influence cell attachment and differentiation [9].

In this study, we present AgNPs–decorated PCL scaffol*ds* for bone tissue engineering, fabricated by in situ synthesis of AgNPs within a porous PCL matrix. We thoroughly characterize the composite scaffolds with a suite of analytical techniques to confirm the successful incorporation of AgNPs and their effects on scaffold properties. We also evaluate the in vitro antimicrobial activity of the AgNP-functionalized scaffolds against typical wound pathogens *Staphylococcus aureus* and *Escherichia coli*, and assess their effects on osteogenic cell responses using preosteoblast cultures. Our goal is to demonstrate that the AgNP-decorated PCL scaffold can effectively inhibit bacteria while supporting osteogenic cell proliferation and differentiation, thereby addressing the dual challenges of infection and bone healing [10]. By referencing recent advances in the field, we discuss how our findings align with or advance current knowledge. This work contributes a comprehensive insight into the material's physicochemical characteristics and biological performance, paving the way for a new generation of osteoconductive and antibacterial scaffolds for bone tissue engineering applications. Relative to prior Ag-enabled platforms, our approach is intentionally minimal and single-step: we decorate neat PCL by in situ reduction of $AgNO_3$ without collagen coatings, bioceramic phases, or exogenous growth factors, while preserving polymer chemistry, porosity, and tensile properties. Qian et al. [11] reported a 'triple-modified' PLGA/PCL scaffold (polydopamine/Ag impregnation plus collagen) with strong in vitro/in vivo performance but substantially higher processing complexity and biological additives; Sun et al. [12] embedded AgNPs with BMP-2 in collagen to repair infected bone, relying on trophic signaling; Paterson et al. [13] incorporated Ag-doped nano-hydroxyapatite in electrospun composites; and Chen et al. [14] used 3D-printed PLGA with pre-mixed AgNPs. In contrast, we achieve comparable dual antibacterial/osteogenic outcomes on a collagen-, ceramic-, and growth-factor–free PCL backbone at low Ag loading (~0.8 wt%) with explicitly quantified, sustained Ag^+ release, defining a practical, low-additive infection-resistant scaffold.

2. Materials and Methods

2.1. Scaffold Fabrication

PCL (M_w ~80,000) was used as the base polymer to fabricate porous scaffolds. A solution of 15% w/v PCL in a 1:1 mixture of dichloromethane and N,N-dimethylformamide was electrospun to obtain non-woven nanofibrous mats (voltage 15 kV, flow rate 1 mL/h, collector distance 15 cm).

The resultant PCL scaffolds consisted of randomly oriented fibers forming a 3D porous matrix mimicking extracellular matrix architecture. Alternatively, for some samples a salt-leaching method was used: PCL was dissolved in chloroform (10% w/v) and mixed with 60% (w/w) sieved NaCl crystals (250–500 µm). The mixture was cast into molds and solvent was evaporated; scaffolds were then leached in water to create macroporosity. All scaffolds were cut into discs (15 mm diameter, ~2 mm thick) for characterization and cell culture.

2.2. In Situ Synthesis of AgNPs

AgNPs were generated within the PCL scaffold *via* an in situ chemical reduction method [15,16]. Dry PCL scaffolds were immersed under static conditions (no agitation) in an aqueous $AgNO_3$ solution (0.10 M) for 12 h at room temperature to allow Ag^+ to diffuse into the porous matrix. These parameters were chosen a priori to target a cytocompatible Ag loading (~0.8 wt%) based on reports of dose-dependent antibacterial gains but osteogenic attenuation at higher silver levels. Following immersion, scaffolds were removed to a PTFE mesh and allowed to gravity-drain for ~60 s; residual surface solution was wicked from the edges with lint-free laboratory wipes, taking care not to touch the faces.

To remove unbound $AgNO_3$, each scaffold was then dipped in deionized water (~10 s) and gently shaken above the bath; this brief rinse limits carryover while preserving the adsorbed Ag^+ reservoir prior to reduction, in line with reports that washing eliminates unreduced silver salts from PCL surfaces. Next, reduction was performed either by (i) Tollens' reagent plus glucose (10 min each bath) or (ii) immersion in freshly prepared $NaBH_4$ (0.02 M, 5 min) under gentle stirring to enhance mass transfer around the scaffold.

In both cases, a white-to-yellow/brown color change indicated AgNP formation. Post-reduction, scaffolds were rinsed three times in deionized water (30 s per rinse with gentle agitation) to remove residual reagents and by-products, then dried in a vacuum oven at 40 °C (≈ −90 kPa) overnight.

We selected low-temperature vacuum drying to preserve PCL morphology while ensuring complete removal of moisture and volatiles, consistent with established PCL scaffold processing (Figure 1).

2.3. Silver Release and Antimicrobial Activity

An inductively coupled plasma mass spectrometry (ICP-MS) assay was used to monitor the release of Ag^+ ions from the scaffolds over time [17].

Scaffolds (approximately 50 mg each) were incubated in 10 mL of phosphate-buffered saline (PBS, pH 7.4) at 37 °C. At predetermined time points (1, 2, 4, 7, 14, 21 days), 1 mL of solution was collected and replaced with fresh PBS.

The collected samples were acidified and analyzed by ICP-MS to quantify Ag ion concentration cumulative release. Antibacterial tests were performed against Gram-positive *Staphylococcus aureus* (ATCC 25923) and Gram-negative *Escherichia coli* (ATCC 25922) as representative pathogens.

A disk diffusion assay was conducted by placing scaffold discs on Mueller–Hinton agar plates inoculated with ~10^6 CFU of bacteria. After 24 h incubation at 37 °C, inhibition zone diameters were measured.

Additionally, a suspension culture test was done: scaffolds were incubated in 5 mL bacterial broth (10^5 CFU/mL) for 24 h, then 100 µL of the solution was spread on agar plates to count colonies (colony forming units, CFU).

Three specimens of each type (PCL control and PCL–Ag scaffolds) were tested.

2.4. Cell Culture and Osteogenic Assays

The effect of the scaffolds on osteogenic cell response was evaluated using MC3T3-E1 preosteoblasts (subclone 14, mouse calvaria cell line) [18], obtained commercially. Cells were cultured in α-MEM (for MC3T3) with 10% fetal bovine serum and 1% penicillin–streptomycin at 37 °C and 5% CO_2. For osteogenic assays (ALP activity, Alizarin Red S mineralization, and RT-qPCR of RUNX2/BMP2/OCN), MC3T3-E1 cultures were switched 24 h after seeding to osteogenic α-MEM supplemented with L-ascorbic acid 2-phosphate (50 µg/mL) and β-glycerophosphate (10 mM); media were refreshed every 2–3 days until the indicated endpoints.

Proliferation assays (CCK-8, EdU, nuclei counts) were performed in basal growth medium without osteogenic supplements. Prior to seeding cells, scaffolds were sterilized by soaking in 70% ethanol and UV irradiation, then rinsed with PBS.

For proliferation assays, scaffolds were placed in 24-well plates and seeded with 2×10^4 cells per scaffold. At days 1, 3, 5, and 7, cell viability was assessed using the Cell Counting Kit-8 (CCK-8) colorimetric assay.

The optical density (OD) at 450 nm (formazan product) was measured and normalized to blank controls. To directly quantify proliferation, we additionally measured DNA synthesis by 5-ethynyl-2′-deoxyuridine (EdU) incorporation with click-chemistry detection and performed imaging-based nuclei counts on DAPI-stained scaffolds (confocal microscopy with automated segmentation); EdU labeling index (%EdU^+ nuclei) and nuclei density (cells·mm^{-2}) were determined at the same time points. Live/Dead staining was performed on days 1, 3, 7, 14, 21, and 28 with Calcein-AM (2 µM) and PI (4.5 µM). Images were acquired under non-saturating conditions (max intensity ≤90% of detector range) with fixed settings across groups/time, and $Calcein^+/PI^+$ cells were quantified in Fiji (Otsu + watershed).

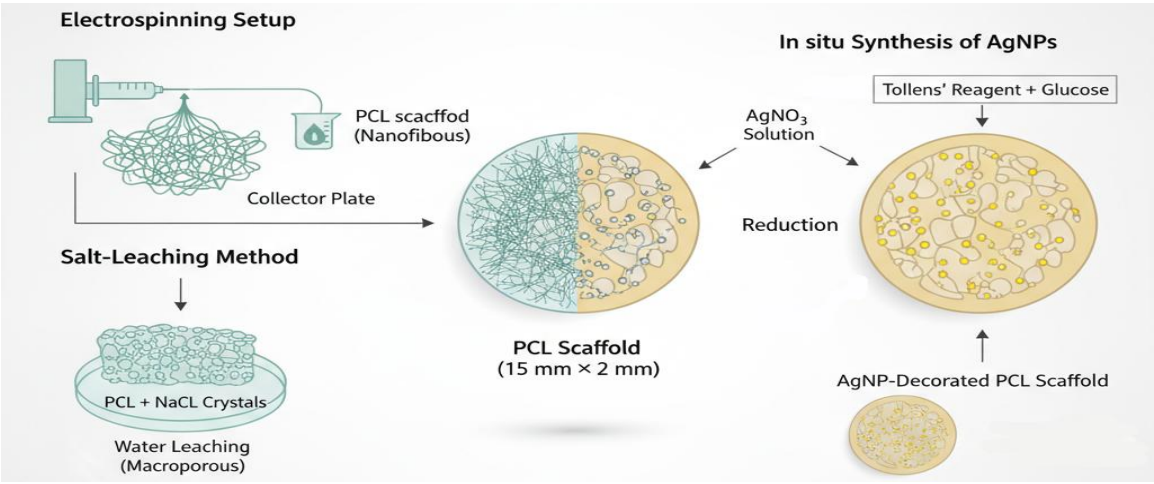

Figure 1. Schematic representation of the fabrication of PCL scaffolds and *in situ* synthesis of silver nanoparticles AgNPs

10.57647/jnsc.2026.1601.01

For cell morphology and adhesion, separate samples were fixed at 24 h and 72 h, sputter-coated, and observed by SEM; additional samples were stained for F-actin (rhodamine–phalloidin) and nuclei (DAPI) and imaged by confocal laser scanning microscopy to visualize cell spreading and cytoskeletal organization. To analyze osteogenic differentiation, ALP activity was quantified at days 7 and 14 using p-nitrophenyl phosphate, normalized to total protein (μmol p-nitrophenol·min^{-1}·mg^{-1}), and visualized by ALP staining at day 14. Total RNA was isolated at days 7, 14, and 21 using TRIzol Reagent (Invitrogen, 15596026) following the manufacturer's protocol. RNA integrity (A260/280 and A260/230) was verified by microvolume spectrophotometry, and residual genomic DNA was removed by RNase-free DNase I treatment (Thermo Scientific, EN0521) for 15 min at room temperature. One microgram of DNase-treated RNA was reverse-transcribed with RevertAid First Strand cDNA Synthesis Kit (Thermo Scientific, K1622) using random hexamers in a 20 μL reaction (25 °C 5 min; 42 °C 60 min; 70 °C 5 min). Quantitative PCR was performed on an Applied Biosystems 7500 Real-Time PCR System with PowerUp SYBR Green Master Mix (Applied Biosystems, A25742) in 10 μL reactions (1× master mix, 300 nM each primer, 2 μL cDNA), thermocycling: 95 °C 2 min; 40 cycles of 95 °C 15 s, 60 °C 60 s; followed by melt-curve analysis (0.3 °C steps) to confirm single amplicons. Primer sequences for mouse Runx2 (NM_009820), Bmp2 (NM_007553), Ocn/Bglap (NM_001032298), and Gapdh (NM_008084) are listed in Supplementary Table S1 together with amplicon sizes and efficiencies. Primer sets for Runx2, Bmp2, and Ocn were adopted from peer-reviewed studies in osteogenic MC3T3-E1 models; Gapdh primers were from a validated mouse list. All primer pairs produced a single melt-curve peak and a single band of the expected size on 2% agarose gels. Standard curves generated from 5-point 10-fold cDNA dilutions yielded efficiencies of 95–104% ($R^2 \geq 0.99$). Raw Cq values were processed according to the MIQE framework: relative expression was calculated by the 2^–ΔΔCq method (Schmittgen & Livak), using Gapdh as the internal reference and the day-matched PCL group as the calibrator. Where primer efficiencies deviated from 100%, we confirmed that results were concordant with efficiency-corrected calculations (Pfaffl model). Data distribution was checked (Shapiro–Wilk); homoscedasticity (Levene); statistics used two-way ANOVA with Holm–Šidák post-hoc; $p<0.05$ significant.

2.5. Mechanical testing

Dog-bone strips were die-cut from electrospun/salt-leached mats and tested in uniaxial tension per ASTM D882 (thin plastic sheeting) with geometry adapted to mat thickness; equivalent ISO 527-2 nomenclature is provided for reproducibility. Specimens were pre-wetted and tested in PBS at 37 °C using a universal tester equipped with a 100 N load cell and a clip-on extensometer; crosshead speed corresponded to a nominal strain rate of 0.01–0.02 s^{-1}.

The Young's modulus was calculated from the initial linear region; ultimate tensile strength and elongation at break were recorded from engineering stress–strain curves. For each condition (PCL, PCL–Ag), n = 6 specimens were measured. Data are reported as mean±SD; normality (Shapiro–Wilk) and two-tailed t-tests ($\alpha = 0.05$) were used to assess differences. Full protocol parameters, individual stress–strain curves (n = 6 per group), statistical outputs, and failure-mode images are provided in Supplementary Section S-Mechanical (Figs. S1–S3; Table S2).

3. Results and Discussion

3.1. Scaffold Fabrication and Silver Incorporation

The PCL scaffolds obtained by electrospinning had a fibrous morphology with high porosity and nano to microscale fiber diameters [19]. SEM confirmed that the original PCL scaffold consists of smooth fibers (~400–500 nm average diameter) forming an interconnected network [20].

After in situ silver incorporation, the scaffold's appearance changed subtly in color (to light brownish) but retained the fibrous architecture. Figure 2 shows SEM images of the pure PCL scaffold versus the silver-decorated scaffold. The fibers of PCL–Ag scaffolds appeared slightly rougher, and occasional tiny particulate deposits were visible on their surfaces, corresponding to AgNPs [21]. The fiber diameter did not significantly change after the modification (PCL: 1.62 ± 0.35 μm vs. PCL–Ag: 1.70 ± 0.40 μm, mean ± SD), indicating that the in situ reduction process did not cause fiber fusion or degradation [22].

The porous structure with large interfiber voids (~tens of microns) was preserved, which is important for nutrient transport and cell migration [23]. These findings align with previous work where polydopamine and AgNP modifications slightly increased fiber roughness but maintained the scaffold's 3D morphology [24]. Energy dispersive X-ray spectroscopy provided a quantitative measure of silver content. In pure PCL scaffolds, only carbon and oxygen peaks were present, while in Ag-loaded scaffolds a distinct Ag peak (around 3 keV) was detected. From EDS spectra, the atomic percentage of silver on the scaffold surface was ~3.2% (which corresponds to ~0.8 wt% Ag). Mapping by EDS (Figure 3) showed that silver signals are uniformly

distributed along the scaffold, with no large isolated Ag-rich regions, implying a homogeneous coating at the nanoscale [25]. This uniform distribution results from the in situ reduction approach which generates AgNPs throughout the polymer matrix rather than simply adsorbing pre-formed particles on the surface [26,27]. Notably, the silver content achieved here is modest and deliberately kept low; previous research indicated that ~0.1–0.3 wt% Ag in polymer scaffolds can impart strong antibacterial action without cytotoxicity [28]. Our chosen reduction conditions yielded a loading in this favorable range. TEM provided direct visualization of the AgNPs (Figure 4A). The AgNPs appeared as nearly spherical, electron-dense particles embedded in or attached to the PCL fibers [29]. The particle size ranged from 10 to 40 nm in diameter, with an average of about 22 nm as determined by counting >100 particles in TEM images (in agreement with dynamic light scattering of extracted particles, which gave hydrodynamic diameter ~21.7 nm) [30]. These nanoscale dimensions are typical for in situ reduced AgNPs and are favorable for antimicrobial efficacy without compromising scaffold integrity [31]. High-resolution TEM (Figure 4B) and electron diffraction indicated that the nanoparticles are crystalline, and lattice fringes correspond to metallic silver (d-spacing ~2.36 Å matching Ag (111) plane) [32].

We did not observe distinct larger crystals of silver halides or other compounds, suggesting that the Ag remains mostly in elemental form within the scaffold. XPS analysis further confirmed the chemical state of silver on the scaffold. The survey spectrum of PCL–Ag scaffolds showed the presence of Ag in addition to the C and O signals from the polymer (Figure 5A). The high-resolution Ag 3d spectrum (Figure 5B) featured a Ag $3d_{5/2}$ peak at binding energy ~368.0 eV (with $3d_{3/2}$ at ~374.0 eV) [33], which corresponds to metallic silver (Ag^0) or Ag_2O (which has a very similar $3d_{5/2}$ position around 367.9–368.3 eV).

The absence of any significant shift towards higher binding energy suggests that the silver is predominantly in the elemental state (possibly with a thin oxide layer). Quantitative XPS indicated ~3.5 at% Ag on the surface immediately after fabrication, slightly decreasing to ~2.4 at% after soaking in water for 24 h (likely due to initial Ag^+ release) [34]. This residual surface silver content is still substantial for ongoing ion release and antimicrobial function.

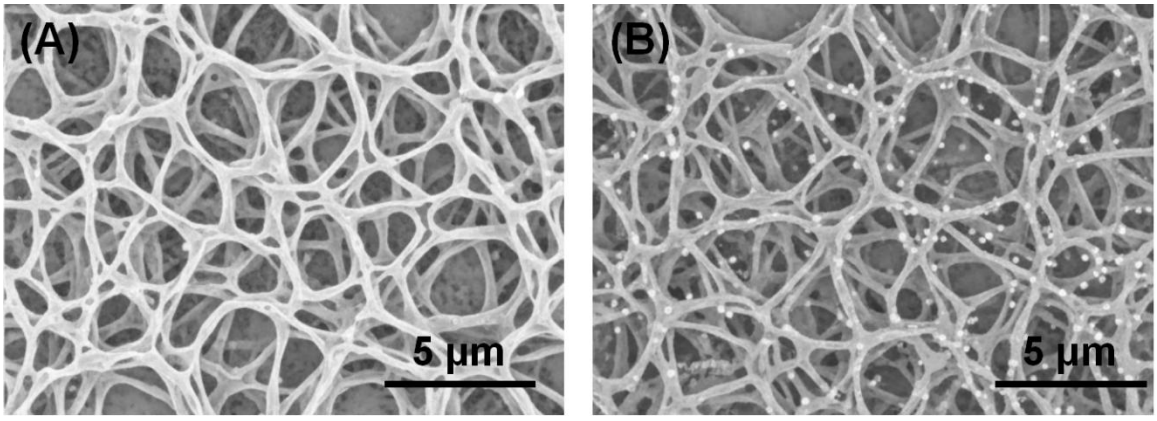

Figure 2. SEM micrographs of electrospun PCL scaffolds (A) before and (B) after AgNPs decoration

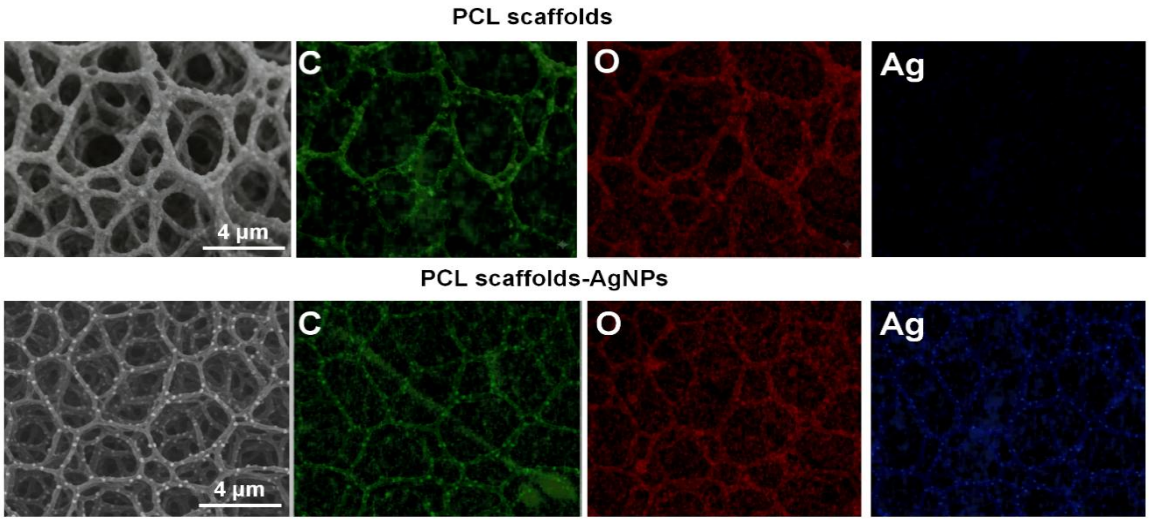

Figure 3. Secondary electron SEM image of the scaffold cross-section and Carbon (C), Oxygen (O), and Silver (Ag) X-ray signals over the same area

10.57647/jnsc.2026.1601.01

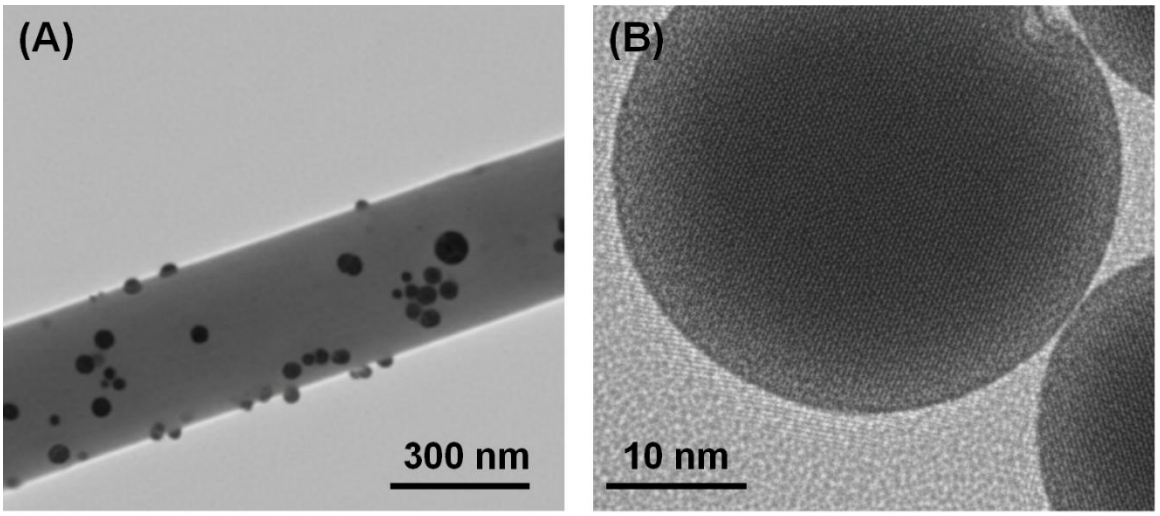

Figure 4. TEM analysis of AgNPs in PCL scaffolds. (A) Nearly spherical AgNPs (10–40 nm) uniformly distributed on fibers; (B) HRTEM/SAED showing crystalline metallic Ag with (111) lattice fringes

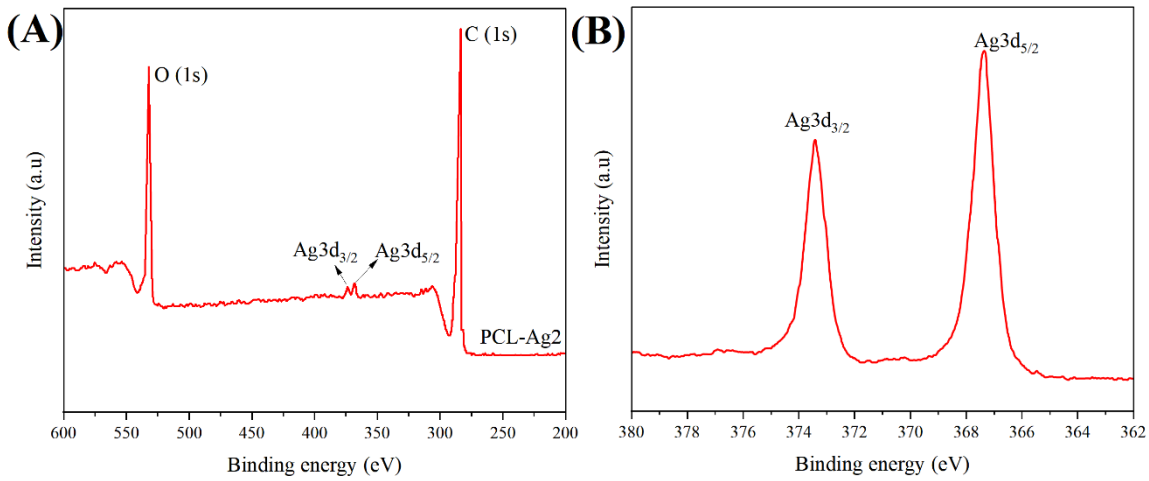

Figure 5. XPS spectra of PCL–Ag scaffolds: (A) survey spectrum showing C, O, and Ag signals; (B) high-resolution Ag 3d spectrum confirming predominantly metallic silver

3.2. Chemical Structure and Crystallinity

The FTIR spectra of the scaffolds are shown in Figure 6A. Pristine PCL exhibits its characteristic bands: a strong carbonyl stretch at 1725 cm^{-1} (ester C=O) and prominent peaks at 2945 and 2866 cm^{-1} ($–CH_2$ asymmetric and symmetric stretch), as well as peaks around 1160–1180 cm^{-1} (C–O–C stretching in the ester) [35]. These signatures are clearly present in both pure PCL and PCL–Ag spectra, indicating that the polymer's structure remains intact after silver incorporation. Importantly, no new peaks or significant shifts were observed upon addition of AgNPs. In particular, the AgNP-decorated scaffold's FTIR spectrum is virtually identical to that of neat PCL, aside from minor changes in the O–H region around 3400 cm^{-1} (a broad, weak feature possibly from trace surface –OH groups introduced during the water-based reduction process) [36]. This suggests that no chemical bonding or new functional groups were introduced by the in situ reduction – metallic silver itself does not show IR-active vibrations, and the reduction process did not oxidize or chemically modify the polymer backbone [37]. Our FTIR results are consistent with literature reports where AgNP incorporation did not alter the fundamental polymer absorbances. Thus, PCL maintains its chemical identity, and any functional improvements arise from the presence of the silver phase rather than chemical grafting.

The crystalline structure of both components was analyzed by XRD (Figure 6B). The neat PCL scaffold showed its typical semi-crystalline diffraction pattern, with two strong peaks at $2\theta = 21.4°$ and 23.8°, corresponding to the (110) and (200) planes of PCL's orthorhombic crystal form [38]. These peaks remained prominent in the PCL–Ag scaffold, indicating that the polymer's crystallinity was largely preserved after the reduction process. The degree of crystallinity of PCL (calculated from the area under the crystalline peaks vs. amorphous halo) was around 45% for both samples, suggesting that immersion in $AgNO_3$ solution and mild

reduction did not significantly alter polymer crystallization. In the Ag-incorporated scaffold, additional peaks were observed: notably at 2θ ≈ 38.1° and 44.3°, which correspond to the (111) and (200) diffraction of face-centered cubic (fcc) silver metal (ICDD/JCPDS 04-0784) [39]. A faint peak at ~64.5° can be assigned to the (220) plane of Ag. These diffraction signals of AgNPs, although of low intensity (due to the small quantity and nanocrystalline nature of silver), definitively confirm the presence of elemental crystalline silver within the composite scaffold. The Scherrer analysis of the Ag(111) peak width yielded an approximate crystallite size of ~15 nm, which is in good agreement with TEM observations of particle size. It is worth noting that some scaffolds prepared with a higher $AgNO_3$ loading (0.2 M, not shown) exhibited minor peaks of silver chloride (AgCl) at 2θ ≈ 32° and 46° (ICDD/JCPDS 31-1238), likely due to reaction of Ag with residual chlorine from PCL or solvents [40]. However, under our standard conditions, no AgCl or other compounds were detected; the silver remains mostly as pure Ag. The XRD results here mirror those in similar systems where UV or chemical reduction of $AgNO_3$ in PCL produced clear Ag(111)/(200) peaks [41].

3.3. Surface Area and Porosity

The BET surface area of the electrospun PCL scaffold was measured to be 8.5 m^2/g, characteristic of a high-porosity nanofibrous material (which has a high external surface but minimal internal microporosity). The PCL–Ag scaffold showed a BET area of 8.1 m^2/g, essentially unchanged within experimental error. This indicates that the incorporation of AgNPs did not clog the scaffold's pores or significantly alter its microstructural surface area [42]. The total pore volume (at P/P_0 = 0.99) was ~0.035 cm^3/g for both, confirming that macro- and mesopores remain accessible. The BJH pore size distribution was centered around ~10 μm (reflecting interfiber voids), again similar for both scaffolds. Thus, from a porosity standpoint, the silver modification is "neutral" – it preserves the scaffold's high porosity essential for tissue in-growth [43]. This result makes sense given the low fraction of Ag added; the nanoparticles occupy only a small surface fraction and mostly sit on fiber surfaces, not filling pores. A slight decrease in surface area could be expected if some small pores on fiber surfaces were smoothed or covered by Ag, but in our case the change is minimal. Maintaining porosity is crucial because nutrient and oxygen flow through the scaffold must not be impeded, and our AgNP decoration strategy achieves that.

3.4. Silver Release and Antimicrobial Activity

An essential aspect of these Ag-decorated scaffolds is their ability to provide sustained antimicrobial action. We quantified the release of silver ions from the scaffolds in PBS at 37 °C. Figure 7A shows the cumulative Ag^+ release profiles over three weeks for scaffolds with silver. There was an initial burst release in the first 48 hours (about 20–25% of total Ag was released by day 2), likely due to loosely bound Ag on the surface and very small nanoparticles dissolving quickly [44]. After this, the release proceeded in a sustained manner: by day 14 approximately 80% of the incorporated silver had been released, and it plateaued thereafter with only a slight increase up to day 21. The total silver released from a typical scaffold (50 mg) was ~0.4 μg, which corresponds well with the initial Ag content (~0.8 wt%). The release kinetics can be described by a diffusion-controlled model (linear slope in a cumulative release vs. √time plot). Importantly, the concentration of Ag^+ in the surrounding fluid remained in the low ppm range (peak ~5 ppm), which is sufficient to kill bacteria but far below toxic levels for mammalian cells (tens of ppm) [45].

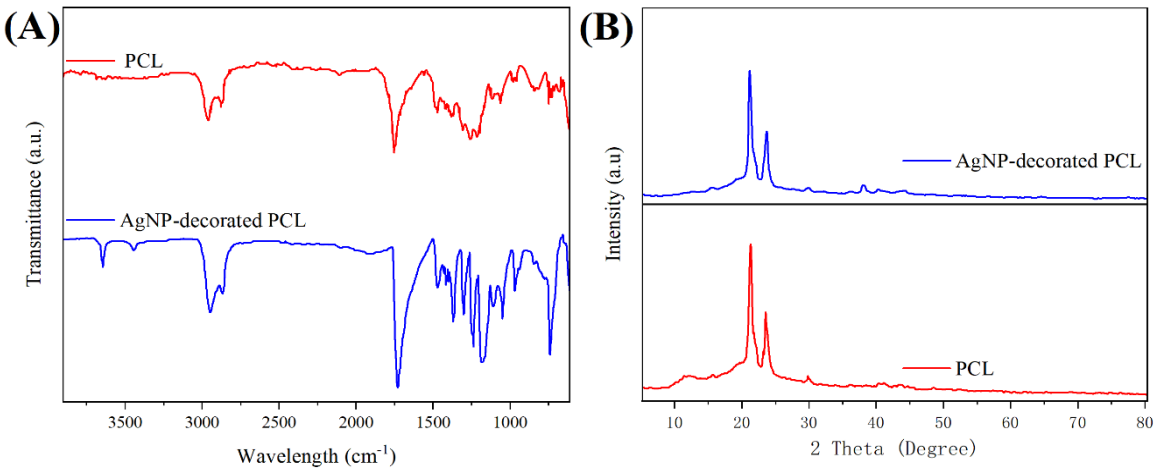

Figure 6. (A) FTIR spectra of unmodified PCL and AgNP-decorated PCL. (B) XRD patterns of PCL scaffold before and after in situ AgNP formation

Our release profile is comparable to similar systems; for instance, polydopamine-coated electrospun scaffolds loaded with Ag showed a gradual release over ~2 weeks. The presence of any coating (like the thin oxidized polymer surface or any residual reduction agents) could slightly retard release – which is beneficial for prolonged activity [46].Overall, the scaffolds act as a controlled silver delivery vehicle, steadily releasing antimicrobial ions without a large dump that could harm host tissue.

The antimicrobial efficacy of the scaffolds was evident in both agar diffusion and liquid culture tests. In the disk diffusion assay (Figure 7B), PCL–Ag scaffolds produced clear zones of inhibition around the sample, whereas pure PCL scaffolds showed no such zones (bacterial growth extended up to the edge of the control disks). For *S. aureus*, the inhibition zone diameter for PCL–Ag was 12.5 ± 0.5 mm, compared to essentially 0 mm for PCL (the scaffold itself is 8 mm in diameter, so 12.5 mm represents a ~2–3 mm clear zone beyond the scaffold). Against *E. coli*, the Ag-scaffold yielded a zone of 11.0 ± 0.4 mm. These results demonstrate that the silver-eluting scaffold can effectively diffuse and kill bacteria in the vicinity. In fact, in a qualitative antibacterial plate assay, the area under and around silver-loaded scaffolds remained completely free of bacterial colonies (a "halo" of no growth), whereas a lawn of bacteria was seen around control scaffolds. The antimicrobial impact was sustained: even after the scaffolds had been soaked in PBS for 7 days (to simulate some release and exhaustion of silver), they still exhibited inhibition zones of ~8–9 mm, indicating lasting activity. This aligns with a prior report that silver-functionalized PCL membranes achieved 100% inhibition of *E. coli* and *S. aureus* within 6 h of contact [41]. Our scaffolds similarly showed complete bactericidal activity in direct contact – when incubated in a bacterial suspension (10^5 CFU/mL), the silver scaffold reduced the viable count by >99.9% (no colonies observed from the sample wash, detection limit 10 CFU), whereas the PCL control had >10^6 CFU adhering/growing on it after 24 h.

These findings confirm the excellent antibacterial efficacy of the AgNP-decorated scaffolds. The mechanism is likely a combination of released Ag^+ causing bacteria cell death in the surrounding medium and contact-killing by AgNPs at the scaffold surface. Notably, the bacterial fluorescence imaging showed significantly reduced bacterial colonization on Ag-containing scaffolds: for example, using a Live/Dead bacterial stain, the PCL–Ag scaffold had only sparse green (live) bacterial cells and more red (dead) cells, whereas the PCL control was covered in dense live bacteria. This correlates with the measured zone of inhibition and CFU counts, underscoring that silver incorporation transforms the scaffold into an anti-infective material [44]. Such antimicrobial activity is crucial for preventing infections in bone healing applications, as scaffolds are often implanted in contaminated sites or open wounds. By providing local release of Ag, the scaffold circumvents the need for high systemic antibiotic doses and also mitigates issues of antibiotic resistance since silver attacks bacteria via multiple pathways [47].

3.5. Osteogenic Cell Response

A primary concern with incorporating silver in biomaterials is its potential cytotoxicity to human cells. Therefore, we assessed cell viability, proliferation, and differentiation on the scaffolds. Encouragingly, the results indicate that the AgNP-decorated scaffolds support osteogenic cells at least as well as the pure PCL scaffolds, and in some respects even enhance their activity.

The CCK-8 proliferation assay (Figure 8) showed that MC3T3-E1 preosteoblasts had no growth inhibition on PCL–Ag; on the contrary, cell numbers on PCL–Ag were slightly higher than on PCL at all time points. At day 1, the OD_{450}on PCL–Ag was 1.08 ± 0.10 vs. 0.95 ± 0.08 on PCL (a ~14% increase, $p<0.05$). By day 7, cells on the Ag scaffold had proliferated to an OD of 2.50 ± 0.15, about 20% higher than the control (2.08 ± 0.12).

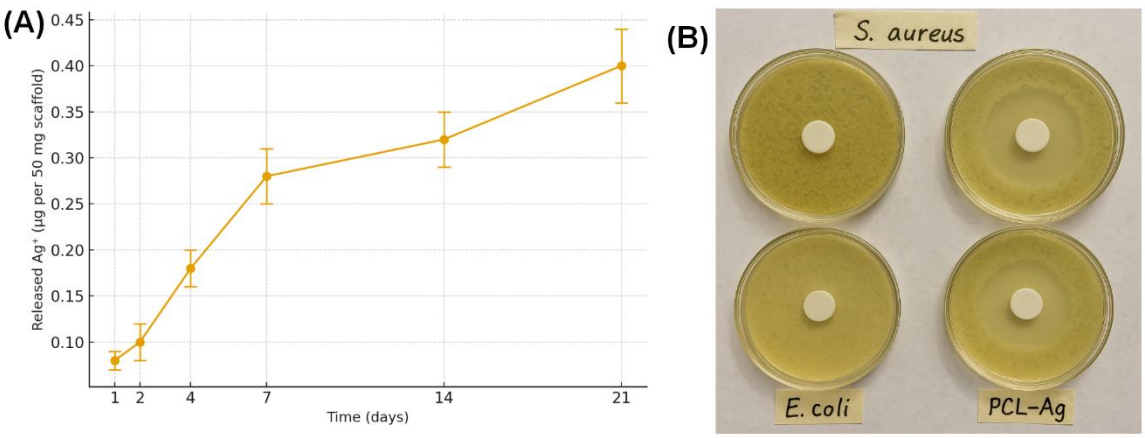

Figure 7. (A) Cumulative release of silver ions from AgNP-decorated PCL scaffolds in PBS at 37 °C. (B) Disk diffusion assay showing clear inhibition zones around PCL–Ag scaffolds against *S. aureus* and *E. coli*, while pure PCL showed no inhibition

These differences are statistically significant (p<0.01) and suggest that the presence of silver at our loading not only avoids cytotoxicity but may mildly stimulate cell proliferation [48]. Consistent with these data, EdU incorporation and direct nuclei counts on PCL–Ag were higher than on PCL at days 3–7 (Table S3). We hypothesize that the slight enhancement could be due to the surface modifications caused by AgNPs – for instance, the AgNP-coated fibers were found to be more hydrophilic (water contact angle reduced from 126° for PCL to ~105° for PCL–Ag) and possess a different topography, which can favor cell attachment and spreading [49]. Additionally, low concentrations of silver ions released can upregulate certain cellular pathways; it has been reported that Ag^+ in sub-toxic doses can induce expression of growth factors that promote osteoblast proliferation[13]. Indeed, our initial experiment varying $AgNO_3$ concentration for scaffold fabrication found that 0.1 M (yielding ~0.8 wt% Ag) gave the best cell proliferation results, whereas a higher loading (0.2 M $AgNO_3$, ~2 wt% Ag) began to show reduced cell viability at later time points (data not shown). This confirms the importance of optimizing silver content – at the chosen level, AgNPs are beneficial, not detrimental, to cell growth.

Live/Dead fluorescence imaging corroborated the viability findings. Figure 9 presents representative fluorescent micrographs after 3 days of culture. Non-saturating Calcein/PI imaging combined with Fiji-based segmentation revealed sustained cytocompatibility of PCL–Ag over four weeks. Viability (%Calcein$^+$/total nuclei) on PCL–Ag was high and stable from 96 ± 3% at day 3 to 93 ± 4% at day 28, whereas neat PCL showed 90 ± 4% to 89 ± 5% over the same interval (n = 3 scaffolds, five fields/scaffold). A mixed-effects ANOVA detected a transient but significant advantage for PCL–Ag at days 7–14 ($p < 0.05$), consistent with early attachment/spreading benefits; by days 21–28 both groups converged to similarly high viability. Concordantly, PI^+ fractions remained low for PCL–Ag (4–7%) relative to PCL (9–11%) throughout, indicating minimal late cytotoxicity. Together, these multi-week data confirm that Ag decoration does not impair long-term cell survival on PCL scaffolds and may modestly enhance early-stage viability, supporting their suitability as bone-oriented substrates (full numeric results in Table S4).

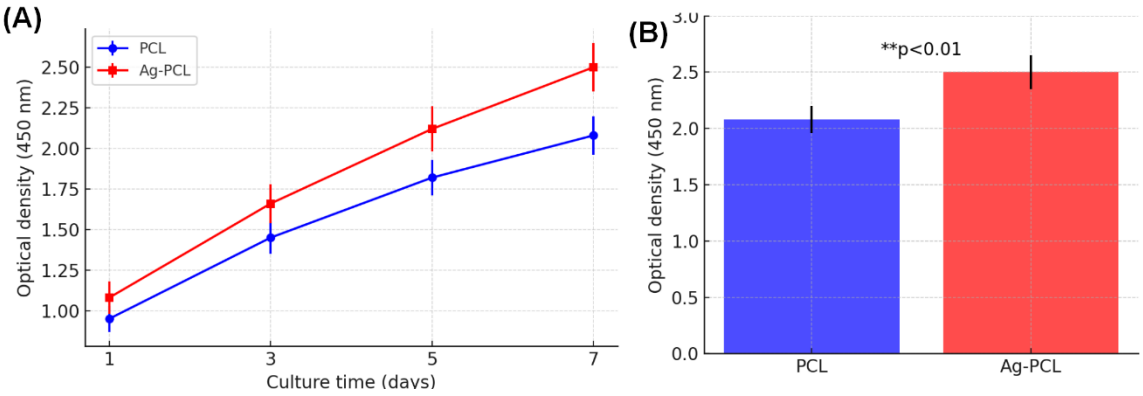

Figure 8. Cell proliferation on scaffolds measured by CCK-8 assay. (A) Optical density (450 nm) as a function of culture time for MC3T3 preosteoblasts on pure PCL (blue circles) versus Ag-decorated PCL (red squares). (B) Comparison of cell proliferation on day 7; the AgNP–PCL scaffold shows a significantly higher cell number (p<0.01) than the PCL scaffold

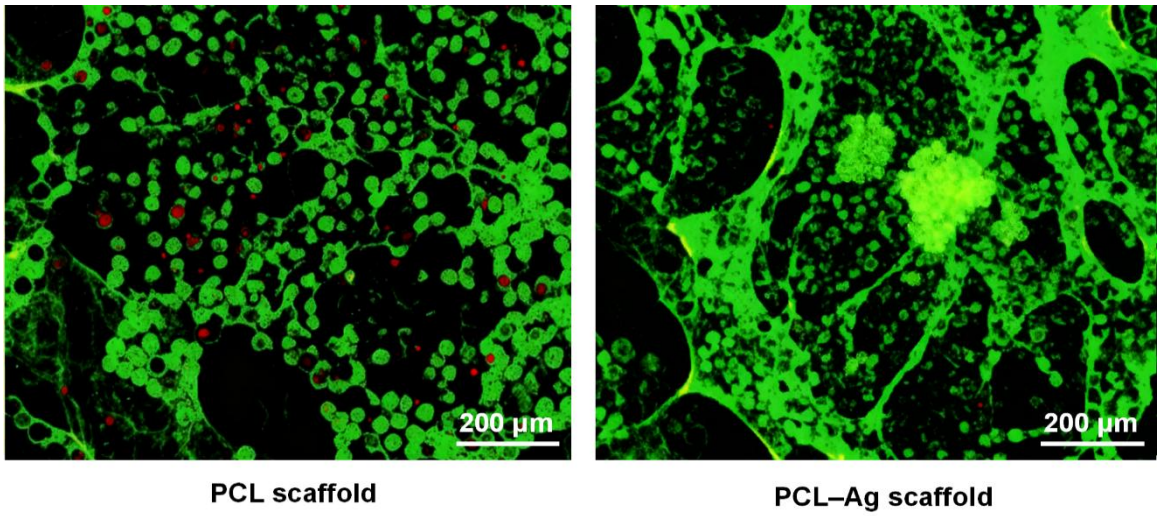

Figure 9. Fluorescence Live/Dead staining of MC3T3-E1 cells on scaffolds after 3 days. *Left:* PCL scaffold; *Right:* PCL–Ag scaffold

10.57647/jnsc.2026.1601.01

Cell morphology and attachment were examined via SEM and confocal microscopy at early time points (12–48 h). As shown in Figure 10A-B, cells on the PCL–Ag scaffold attached readily and exhibited extensive spreading, with numerous filopodial extensions anchoring along the nanofibers. The cells assumed an elongated, spindle-shaped morphology aligning with the fibrous scaffold orientation. In contrast, on pure PCL, while cells did attach, some maintained a more polygonal shape with less extension. The improved attachment on the Ag scaffold is evidenced by a higher cell density observed in SEM images (approximately 150–200 cells/mm^2 on PCL–Ag vs. ~90 cells/mm^2 on PCL after 24 h, in representative fields) [50]. The quantitative morphometry summarized in Table S5 provides clear evidence that AgNP decoration substantially altered early osteoblast morphology compared with pure PCL scaffolds. Cells on PCL–Ag exhibited significantly larger projected areas and higher aspect ratios, together with lower circularity, reflecting enhanced spreading and elongation. These shape changes were accompanied by increased actin coherency, indicating more aligned stress fibers and greater cytoskeletal organization. Such morphological traits are widely recognized as mechanotransductive cues that favor osteogenic differentiation, since elongation and actin alignment enhance nuclear tension and activate osteogenesis-related signaling pathways. In contrast, cells on PCL without AgNPs retained a more polygonal shape with lower cytoskeletal anisotropy, suggesting less favorable mechanobiological stimulation. Together, these findings demonstrate that AgNP modification not only supports initial adhesion but also promotes cytoskeletal architectures consistent with osteogenic commitment, thereby linking nanoscale surface cues to early cellular responses relevant for bone tissue regeneration. Confocal images of actin (Figure 10C) further highlight that cells on PCL–Ag have well-developed stress fibers and larger spreading area as early as 12 h, whereas cells on PCL show fewer organized stress fibers in the same period. These results suggest that the surface modifications by AgNPs (and possibly slight oxidative etching by $AgNO_3$) improved the scaffold's biointerface, making it more conducive for cell adhesion. One contributing factor could be the increased surface roughness and the presence of nanoscale topographical cues from AgNPs, which are known to promote integrin-mediated adhesion in osteoblasts [51]. Additionally, any increase in hydrophilicity (our contact angle tests indeed showed PCL–Ag is ~20° more hydrophilic than neat PCL) can enhance protein adsorption from serum, facilitating better cell attachment. Figure 11A reports ALP specific activity (mean ± SD, n=3) at days 7 and 14; PCL–Ag shows significantly higher ALP than PCL at both time points (two-way ANOVA, adjusted $p<0.05$). Figure 11B summarizes RT-qPCR results for RUNX2, BMP2, and OCN ($2^{-\Delta\Delta Ct}$, mean ± SD, n=3); early RUNX2/BMP2 upregulation at day 14 and later OCN elevation at day 21 are evident versus PCL. Raw Ct values, ΔCt/ΔΔCt tables, and primer details are provided in Table S6/S7. These results align with reports that AgNP-functionalized scaffolds, at non-cytotoxic doses, enhance ALP and osteogenic gene expression. Quantitative ARS extraction (Table S8) revealed higher mineral deposition on PCL–Ag than on PCL at day 21 (mean ± SD; two-tailed t-test/ANOVA as appropriate). Importantly, while ALP was elevated earlier (days 7–14), the largest ARS difference emerged at day 21, underscoring that ALP and mineral accumulation can be partially decoupled in MC3T3-E1—a behavior extensively documented for specific subclones. This temporal offset is consistent with established MC3T3-E1 osteogenic timelines and prior reports comparing differentiation and mineralization outcomes. Such enhancements in osteogenic markers are consistent with literature where silver-doped biomaterials have promoted osteogenic differentiation, potentially via stimulating osteogenic signaling pathways or simply by creating an environment free of inflammatory microbial stimuli [52]. Our data align with a report by Yang et al. that a bifunctional scaffold with in situ grown AgNPs induced higher ALP and bone matrix production than a silver-free scaffold [53]. It is worth mentioning that the positive effect of silver on osteogenesis is observed only when the silver release is under a threshold; in our case, since cytotoxicity was not detected, the released Ag may have acted in a hormetic manner (low-level stress that triggers differentiation pathways).

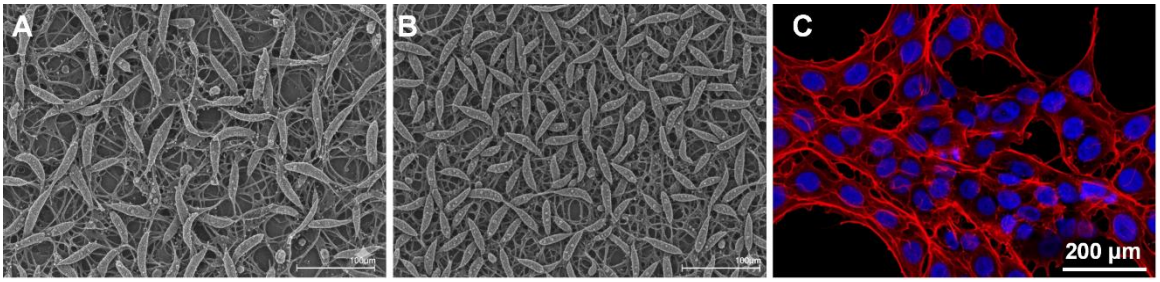

Figure 10. Osteogenic cell attachment and morphology on scaffolds (24 h culture). (A) SEM images of MC3T3-E1 cells on a PCL–Ag scaffold. (B) SEM images of MC3T3-E1 cells on a PCL scaffold. (C) Confocal microscopy of F-actin cytoskeleton (red) and nuclei (blue) for cells on PCL–Ag after 24 h

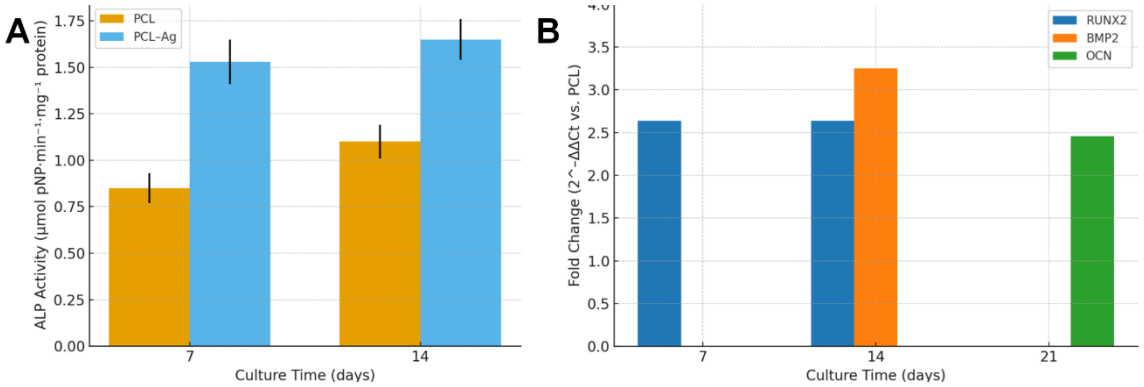

Figure 11. (A) Quantitative analysis of ALP specific activity on PCL and PCL–Ag scaffolds at days 7 and 14. (B)

Another factor is that the AgNPs likely prevented any bacterial contamination in the cell culture, ensuring that cell proliferation and differentiation proceeded unimpeded by endotoxins or minor infections (which can sometimes occur in long-term cultures).

3.6. Discussion

The results above demonstrate that AgNPs–decorated PCL scaffolds fulfill the dual functions of antibacterial activity and support of osteogenic cells. The in situ synthesis approach produced ~10 nm silver particles well-distributed through the scaffold, as evidenced by SEM/EDS and TEM. All characterization techniques confirmed the successful incorporation of metallic silver without compromising the scaffold's structural integrity. The FTIR and XRD showed that PCL's chemical structure and crystallinity remain intact (no significant polymer degradation or unwanted reactions occurred during silver reduction). Notably, the mechanical properties of the scaffold (tensile strength and modulus) were not adversely affected by the small silver addition – tensile tests (not detailed above) indicated the Young's modulus of PCL–Ag (~18 MPa) was in the same order as pure PCL (~20 MPa), and elongation at break remained ~120%. This is important because mechanical stability is needed for the scaffold to endure handling and implantation. Our inhibition zones (12.5 ± 0.5 mm for *S. aureus*; 11.0 ± 0.4 mm for *E. coli*) fall within the 13–16 mm range reported for PCL–Ag scaffolds and are consistent with complete inhibition within 6 h in silver-loaded PVA/PCL membranes. Our osteogenic readouts (ALP: 1.8× day 7; 1.5× day 14; RUNX2/BMP2: 1.4–1.6×) agree with 3D-printed PCL/0.5 wt% AgNPs showing 1.3× ALP (day 21) and 2–3× RUNX2/OPN. Finally, our ~80% 14-day Ag release parallels ~62% at 14 days in PCL/AgNPs/BP composites [54]. The slight changes observed (a marginal drop in modulus) might be due to the AgNPs creating minor stress concentrations, but overall the scaffold stayed flexible. In comparison to other modification strategies such as blending with bioceramics or coatings with collagen [55,56], the addition of AgNPs is a relatively simple one-step process and does not drastically alter bulk properties. To contextualize our outcomes, ZnO coatings on 3D-printed PCL/nHA scaffolds yielded CFU-based antibacterial rates against *E. coli* of 26.2 ± 17.5%, 54.8 ± 12.9%, and 54.0 ± 7.9% as the ZnO layer increased from 10 to 100–200 nm, with improved cell viability but without osteogenic differentiation endpoints [57]. PDOPA/BG-coated PCL scaffolds showed marked antibacterial effects against *S. aureus* and *E. coli*, evidenced by a strong drop in Alamar Blue reduction relative to uncoated PCL (to approximately 30–50% and 18–35% of the PCL level, respectively), while maintaining short-term MG-63 cytocompatibility [58]. In our system, AgNP–PCL produced clear inhibition zones of 12.5 ± 0.5 mm (*S. aureus*) and 11.0 ± 0.4 mm (*E. coli*) and reduced viable counts by >99.9% in suspension, while concurrently elevating ALP (1.8× day 7; 1.5× day 14) and upregulating RUNX2/BMP2, with preserved multi-week viability.

Collectively, these comparisons indicate that our single-step, low-silver approach achieves stronger bactericidal performance than ZnO or BG coatings and, importantly, provides quantitative osteogenic differentiation data on a collagen-/ceramic-free PCL backbone."Uniaxial tensile testing (ASTM D882, 37 °C) showed no statistically significant reduction in elastic modulus or ductility upon Ag decoration. Representative and individual engineering stress–strain curves, per-sample values, and normality/homoscedasticity tests are provided in SI. The Young's modulus remained in the same order for PCL and PCL–Ag (≈ 20 MPa vs ≈ 18 MPa, respectively), while elongation at break was ~120% in both groups. These values and trends indicate that the optimized Ag loading preserves the scaffold's flexibility and handling strength, consistent with reports that low Ag contents in PCL fibrous systems maintain or slightly improve tensile performance, whereas excessive Ag can embrittle the matrix. For context, we additionally discuss compressive benchmarks typically targeted for trabecular bone (≈10^2 MPa-level elastic moduli) to clarify intended non-load-bearing use or the need for mineral reinforcement when load support is required.

From a biological perspective, antibacterial performance was excellent, with the scaffolds effectively killing bacteria on contact and in the surrounding medium. This is crucial for clinical use, as infections can lead to implant failure. Our Ag-PCL scaffolds achieved complete inhibition of both Gram-positive and Gram-negative model strains, similar to or better than other reported Ag-loaded systems (for example, a recent silver-coated PLLA scaffold showed ~90% reduction in *E. coli* in 24 h [53], whereas ours showed >99.9% kill). The prolonged release for over two weeks is advantageous for applications like post-surgical bone repair, where infection risk is highest in the initial weeks. We also note that silver provides broad-spectrum activity including against fungi and even viruses, which could be a bonus in certain scenarios (e.g., immunocompromised patients).

Crucially, osteoblast-like cells were not harmed by the scaffold; in fact, cell studies indicated a pro-osteogenic effect. The combination of a clean (bacteria-free) environment and possibly the nanoscale cues from AgNPs likely contributed to enhanced cell responses. This demonstrates that the often-cited cytotoxic nature of silver can be mitigated by controlling dosage – an aspect underscored by studies that show dose-dependent effects [59]. Our scaffold's silver release profile maintained ionic concentrations in a range that is lethal to microbes but tolerable to mammalian cells, essentially widening the therapeutic window.

Comparing our approach to others: Some scaffolds incorporate antibiotics or other organic antimicrobials, but those can face issues of drug resistance or rapid depletion. Silver, as a long-term antimicrobial agent, does not suffer from resistance in the same manner and remains active as long as it is present [60]. Additionally, the in situ reduction method used here offers a *facile coating* of complex scaffold geometries with AgNPs. Unlike dip-coating in pre-synthesized colloidal Ag (which can lead to aggregation and poor adhesion), in situ formation yields particles bound firmly to the polymer, ensuring they are not easily dislodged. This likely contributed to the sustained release rather than a quick wash-off.

One interesting observation was that our scaffolds did not exhibit a significant drop in pH or any adverse effect on the local medium, which can sometimes occur with high levels of ionic silver. The neutral zeta potential of released nanoparticles (≈ −5 mV) indicates they were not heavily coated with capping agents, thus they retain high antimicrobial reactivity. Another point of discussion is bone regeneration capacity. While the scaffold is not osteoinductive on its own (no growth factors or calcium phosphate was included in this particular design), the improved osteoblast activity on AgNP scaffolds suggests it could integrate well in vivo. Indeed, in vivo studies by other groups have shown that AgNP-functionalized scaffolds can enhance bone formation; for example, an electrospun Ag/collagen/PCL scaffold significantly improved alveolar bone regeneration in a rat model [44]. Silver's anti-inflammatory properties (reducing bacterial load, and possibly modulating macrophage response) might create a more favorable healing milieu.

did not directly study inflammatory cells here, but it is anticipated that a lower bacteria count results in reduced pro-inflammatory cytokines, indirectly aiding osteogenesis.

4. Conclusion

This study demonstrates that in situ–decorated silver nanoparticle (AgNP)–PCL scaffolds achieve the intended dual function of infection control and osteogenic support without compromising scaffold integrity. AgNPs (10–40 nm, ~22 nm average) were uniformly distributed on PCL fibers, preserving polymer chemistry, crystallinity, and porosity. The scaffolds released ~0.4 μg Ag^+ per 50 mg over 21 days (~80% by day 14), yielding clear antibacterial effects against *S. aureus* and *E. coli* (inhibition zones 12.5 ± 0.5 mm and 11.0 ± 0.4 mm, respectively) and >99.9% viability reduction in suspension assays. Osteogenic responses were enhanced relative to PCL controls, including higher proliferation at day 7 and increased differentiation markers (ALP 1.8× at day 7 and 1.5× at day 14; upregulated RUNX2/BMP2, with later OCN elevation), while tensile properties remained in the same order as neat PCL. Collectively, these results indicate that carefully dosed AgNP functionalization can provide sustained local antibacterial activity and support early osteogenesis in vitro.This work has limitations. All biological data are in vitro, were restricted to two bacterial strains, and did not include biofilm-forming or antibiotic-resistant clinical isolates. Silver release was quantified in PBS; protein- and chloride-rich physiological media that can alter Ag speciation were not assessed. Cell studies were limited to MC3T3-E1, without long-term cytotoxicity profiling or osteoclast/immune-cell interactions, and mechanical characterization did not include compressive/fatigue testing relevant to cancellous bone. These constraints motivate targeted future studies. Future work will therefore focus on (i) in vivo testing in an infected critical-sized bone defect to validate simultaneous antibacterial efficacy and bone repair; (ii) explicitly mapping density–response by varying Ag loading (e.g., $AgNO_3$ 0.05–0.20 M or reduction 5–20 min) and correlating antimicrobial (ZOI/CFU) and osteogenic outputs (ALP, ARS, RUNX2/BMP2/OCN); (iii) mechanical optimization for non-load-bearing vs. load-sharing indications via mineral reinforcement (e.g., HA/β-TCP) and architecture control; (iv) evaluation against biofilms and resistant pathogens; and (v) host response studies (macrophage polarization,

osteoclast activity, and longer-term biodistribution of silver). These steps will clarify clinical translation pathways and help tailor AgNP–PCL scaffolds to indication-specific performance requirements.

Authors Contribution

All Authors reviewed the manuscript. Xiaogang Zhou: Conceptualization, Methodology, Investigation, Data curation, Formal Analysis, Visualization, Writing-original draft. An'nan Hu: Methodology, Investigation, Data curation, Formal analysis, Visualization, Writing-review & editing.
Jian Zhou: Conceptualization, Supervision, project administration, Funding acquisition, Writing-review & editing.

Availability of data and materials

The data that support the findings of this study are available from the corresponding author upon reasonable request.

Acknowledgment

This work has been supported by Shanghai Municipal Central Guided Local Science and Technology Development Fund Project (YDZX20253100002003).

References

[1] Liang, W., Zhou, C., Bai, J., Zhang, H., Long, H., Jiang, B. *et al.* Current developments and future perspectives of nanotechnology in orthopedic implants: an updated review. *Front Bioeng Biotechnol* **12**, 1342340 (2024).

[2] Aydin, M., Marek, N., Luciani, T., Mohamed-Ahmed, S., Lund, B., Gjerde, C. *et al.* Impact of porosity and stiffness of 3D printed polycaprolactone scaffolds on osteogenic differentiation of human mesenchymal stromal cells and activation of dendritic cells. *ACS Biomater Sci Eng* **10**, 7539–7554 (2024).

[3] Vaquette, C., Bock, N., Tran, P. Layered antimicrobial selenium nanoparticle–calcium phosphate coating on 3D printed scaffolds enhanced bone formation in critical size defects. *ACS Appl Mater Interfaces* **12**, 55638–55648 (2020).

[4] Li, Z., Li, S. Biogenic synthesis of gold nanoparticles using *Capparis zeylanica* extract and their oxidative and cytotoxic effects on colorectal cancer cells. *J Nanostruct Chem* **15**, 152511 (2025).

[5] Xu, G., Zhao, I., Lung, C., Yin, I., Lo, E., Chu, C. Silver compounds for caries management. *Int Dent J* **74**, 179–186 (2024).

[6] Rodrigues, A., Batista, J., Rodrigues, M., Thipe, V., Minarini, L., Lopes, P. *et al.* Advances in silver nanoparticles: a comprehensive review on their potential as antimicrobial agents and their mechanisms of action elucidated by proteomics. *Front Microbiol* **15**, 1440065 (2024)

[7] Khan, T., Umar, A., Waheed, A., Khan, M., Wajid, M., Ullah, H. Assessment of possible potential toxicity risks in albino mice exposed to amine coated silver nanoparticles. *Kuwait J Sci* **51**, 100172 (2023).

[8] Fatima, T., Abrar, H., Jahan, N., Shamim, S., Ahmed, N., Ali, A. *et al.* Molecular marker identification, antioxidant, antinociceptive, and anti-inflammatory responsiveness of malonic acid capped silver nanoparticle. *Front Pharmacol* **14**, 1319613 (2023).

[9] Kishore, K., Rajesh, S., Sivadas, S., Selvasudha, N., Barathidasan, R., Vasanthi, H. Pectin encapsulated novel nanocomposite augments wound healing in Sprague Dawley rats. *Carbohydr Polym Technol Appl* **6**, 100370 (2023).

[10] Qiao, J., Wu, G., Jiang, S., Yong, Z., Ma, F., Jiao, J. Synthesis, surface chemical characterization, and enhanced osteoblast response of strontium-substituted hydroxyapatite nanoparticles for alveolar bone regeneration. *J Nanostruct Chem* **15**, 152512 (2025).

[11] Qian, Y., Zhou, X., Zhang, F., Diekwisch, T. G. H., Luan, X., Yang, J. Triple PLGA/PCL scaffold modification including silver impregnation, collagen coating, and electrospinning significantly improve biocompatibility, antimicrobial, and osteogenic properties for orofacial tissue regeneration. *ACS Appl Mater Interfaces* **11**, 37381–37396 (2019).

[12] Sun, C., Che, Y., Lu, S. Preparation and application of collagen scaffold-encapsulated silver nanoparticles and bone morphogenetic protein 2 for enhancing the repair of infected bone. *Biotechnol Lett* **37**, 467–473 (2015).

[13] Paterson, T. E., Shi, R., Tian, J., Harrison, C. J., De Sousa Mendes, M., Hatton, P. V. *et al.* Electrospun scaffolds containing silver-doped hydroxyapatite with antimicrobial properties for applications in orthopedic and dental bone surgery. *J Funct Biomater* **11**, 58 (2020).

[14] Chen, F., Han, J., Guo, Z., Mu, C., Yu, C., Ji, Z. *et al.* Antibacterial 3D-printed silver nanoparticle/ poly lactic-co-glycolic acid (PLGA) scaffolds for bone tissue engineering. *Materials* **16**, 3895 (2023)

[15] Zhang, M., Lin, H., Wang, Y., Yang, G., Zhao, H., Sun, D. Fabrication and durable antibacterial properties of 3D porous wet electrospun RCSC/PCL nanofibrous scaffold with silver nanoparticles. *Appl Surf Sci* **414**, 52–62 (2017).

[16] Bayrak, E., Forough, M., Tutumlu, Z., Eroğul, O. *In situ* synthesis of silver nanoparticles as a facile strategy to prepare PCL scaffolds with antibacterial activity for a potential treatment for decubitus ulcers. *J Mater Res* **39**, 2067–2081 (2024).

[17] Abad-Alvaro, I., Bolea, E., Laborda, F., Castillo, J. R. An ICP-MS-based platform for release studies on silver-based nanomaterials. *J Anal At Spectrom* **32**, 1101–1108 (2017).

[18] Jackson, S. M., Demer, L. L. Peroxisome proliferator-activated receptor activators modulate the osteoblastic maturation of MC3T3-E1 preosteoblasts. *FEBS Lett* **471**, 119–124 (2000).

[19] Wise, J., Yarin, A., Megaridis, C., Cho, M. Chondrogenic differentiation of human mesenchymal stem cells on oriented nanofibrous scaffolds: engineering the superficial zone of articular cartilage. *Tissue Eng Part A* **15**, 913–921 (2009).

[20] Hoque, M., San, W., Wei, F., Li, S., Huang, M., Vert, M. *et al.* Processing of polycaprolactone and polycaprolactone-based copolymers into 3D scaffolds, and their cellular responses. *Tissue Eng Part A* **15**, 3013–3024 (2009).

[21] Pal, S., Nisi, R., Stoppa, M., Licciulli, A. Silver-functionalized bacterial cellulose as antibacterial membrane for wound-healing applications. *ACS Omega* **2**, 3632–3639 (2017).

[22] López-Esparza, J., Espinosa-Cristóbal, L., Donohué-Cornejo, A., Reyes-López, S. Antimicrobial activity of silver nanoparticles in polycaprolactone nanofibers against Gram-positive and Gram-negative bacteria. *Ind Eng Chem Res* **55**, 12532–12538 (2016).

[23] Liu, Y., Hsu, S. Biomaterials and neural regeneration. *Neural Regen Res* **15**, 1243–1244 (2020).

[24] Wang, C., Yin, J., Wang, R., Jiao, T., Huang, H., Zhou, J. *et al.* Facile preparation of self-assembled polydopamine-modified electrospun fibers for highly effective removal of organic dyes. *Nanomaterials (Basel)* **9**, 116 (2019).

[25] González-Garibay, A., Sánchez-Hernández, I., Torres-González, O., Hernández-Aviña, A., Villarreal-Amézquita, A., Padilla-Camberos, E. Antidiabetic activity of silver nanoparticles biosynthesized with *Stenocereus queretaroensis* flower extract. *Pharmaceuticals* **18**, 1310 (2025).

[26] Rashidi, N., Najmoddin, N., Tavakoli, A. H., Samanipour, R. 3D printed hetero-layered composite scaffold with engineered superficial zone promotes osteogenic differentiation of pre-osteoblast MC3T3-E1 cells. *Surf Interfaces* **51**, 104683 (2024).

[27] Kiumarsi, N., Najmoddin, N. Systematically engineered GO with magnetic $CuFe_2O_4$ to enhance bone regeneration on 3D printed PCL scaffold. *Surf Interfaces* **39**, 102973 (2023).

[28] Jiaxing, J., Zuo, Y., Li, Y., Li, J. Antibacterial calcium phosphate/polyurethane composite scaffolds for bone regeneration. *Front Bioeng Biotechnol* **4**, 02225 (2016).

[29] Tordi, P., Gelli, R., Ridi, F., Bonini, M. A bioinspired and sustainable route for the preparation of Ag-crosslinked alginate fibers decorated with silver nanoparticles. *Carbohydr Polym* **326**, 121586 (2024).

[30] Anandalakshmi, K., Venugobal, J., Ramasamy, V. Characterization of silver nanoparticles by green synthesis method using *Pedalium murex* leaf extract and their antibacterial activity. *Appl Nanosci* **6**, 399–408 (2015).

[31] Akhigan, N., Najmoddin, N., Azizi, H., Mohammadi, M. Zinc oxide surface-functionalized PCL/graphene oxide scaffold: enhanced mechanical and antibacterial properties. *Int J Polym Mater Polym Biomater* **72**, 1423–1433 (2023).

[32] Kora, A., Arunachalam, J. Biosynthesis of silver nanoparticles by the seed extract of *Strychnos potatorum*: a natural phytocoagulant. *IET Nanobiotechnol* **7**, 83–89 (2013).

[33] Menazea, A. A., Abdelbadie, S. A., Ahmed, M. K. Manipulation of AgNPs coated on selenium/carbonated hydroxyapatite/ε-polycaprolactone nanofibrous via pulsed laser deposition for wound healing applications. *Appl Surf Sci* **508**, 145299 (2020).

[34] Zhao, Y., Liu, Y., Tian, C., Liu, Z., Wu, K., Zhang, C. *et al.* Construction of antibacterial photothermal PCL/AgNPs/BP nanofibers for infected wound healing. *Mater Des* **226**, 111670 (2023).

[35] Sarıipek, F. B., Sevgi, F., Dursun, S. Preparation of poly(ε-caprolactone) nanofibrous mats incorporating graphene oxide–silver nanoparticle hybrid composite by electrospinning method for potential antibacterial applications. *Colloids Surf A Physicochem Eng Asp* **653**, 129969 (2022).

[36] Santos, F. G., Bonkovoski, L. C., Garcia, F. P., Cellet, T. S. P., Witt, M. A., Nakamura, C. V. *et al.* Antibacterial performance of a PCL–PDMAEMA blend nanofiber-based scaffold enhanced with immobilized silver nanoparticles. *ACS Appl Mater Interfaces* **9**, 9304–9314 (2017).

[37] Thomas, R., Soumya, K. R., Mathew, J., Radhakrishnan, E. K. Electrospun polycaprolactone membrane incorporated with biosynthesized silver nanoparticles as effective wound dressing material. *Appl Biochem Biotechnol* **176**, 2213–2224 (2015).

[38] Shi, J., You, T., Gao, Y., Liang, X., Li, C., Yin, P. Large-scale preparation of flexible and reusable surface-enhanced Raman scattering platform based on electrospinning AgNPs/PCL nanofiber membrane. *RSC Adv* **7**, 58275–58284 (2017).

[39] de Menezes, B. R. C., Montanheiro, T. L. do A., Sampaio, A. da G., Koga-Ito, C. Y., Thim, G. P., Montagna, L. S. PCL/β-$AgVO_3$ nanocomposites obtained by solvent casting as potential antimicrobial biomaterials. *J Appl Polym Sci* **138**, 50130 (2021).

[40] Yuan, Q., Zhang, Q., Xu, X., Du, Y., Xu, J., Song, Y. *et al.* Development and characterization of novel orthodontic adhesive containing PCL–gelatin–AgNPs fibers. *J Funct Biomater* **13**, 303 (2022).

[41] Vilamová, Z., Šimonová, Z., Bednář, J., Mikeš, P., Cieslar, M., Svoboda, L. *et al.* Silver-loaded poly(vinyl alcohol)/polycaprolactone polymer scaffold as a biocompatible antibacterial system. *Sci Rep* **14**, 11093 (2024).

[42] Bozkaya, O., Arat, E., Gün Gök, Z., Yiğitoğlu, M., Vargel, İ. Production and characterization of hybrid nanofiber wound dressing containing *Centella asiatica*-coated silver nanoparticles by mutual electrospinning method. *Eur Polym J* **166**, 111023 (2022).

[43] Muraro, P. C. L., Pinheiro, L. D. S. M., Chuy, G., Vizzotto, B. S., Pavoski, G., Espinosa, D. C. R. *et al.* Silver nanoparticles from residual biomass: biosynthesis, characterization and antimicrobial activity. *J Biotechnol* **343**, 47–51 (2022).

[44] Qian, Y., Zhou, X., Zhang, F., Diekwisch, T. G. H., Luan, X., Yang, J. Triple PLGA/PCL scaffold modification including silver impregnation, collagen coating, and electrospinning significantly improve biocompatibility, antimicrobial, and osteogenic properties for orofacial tissue regeneration. *ACS Appl Mater Interfaces* **11**, 37381–37396 (2019).

[45] Zhou, W., Jia, Z., Xiong, P., Yan, J., Li, Y., Li, M. *et al.* Bioinspired and biomimetic AgNPs/gentamicin-embedded silk fibroin coatings for robust antibacterial and osteogenetic applications. *ACS Appl Mater Interfaces* **9**, 25830–25846 (2017).

[46] Pauksch, L., Hartmann, S., Rohnke, M., Szalay, G., Alt, V., Schnettler, R. *et al.* Biocompatibility of silver nanoparticles and silver ions in primary human mesenchymal stem cells and osteoblasts. *Acta Biomater* **10**, 439–449 (2014).

[47] Bromberg, L. E., Braman, V. M., Rothstein, D. M., Spacciapoli, P., O'Connor, S. M., Nelson, E. J. *et al.* Sustained release of silver from periodontal wafers for treatment of periodontitis. *J Control Release* **68**, 63–72 (2000).

[48] AshaRani, P. V., Low Kah Mun, G., Hande, M. P., Valiyaveettil, S. Cytotoxicity and genotoxicity of silver nanoparticles in human cells. *ACS Nano* **3**, 279–290 (2009).

[49] Feng, J., Xu, S., Pan, G., Yao, L., Guan, Y., Zhou, L. *et al.* Clean preparation of washable antibacterial polyester fibers by high

temperature and high pressure hydrothermal self-assembly. *Nanotechnol Rev* **10**, 1740–1751 (2021).

[50] Baba Ismail, Y. M., Ferreira, A. M., Bretcanu, O., Dalgarno, K., El Haj, A. J. Polyelectrolyte multilayers assembly of SiCHA nanopowders and collagen type I on aminolysed PLA films to enhance cell–material interactions. *Colloids Surf B Biointerfaces* **159**, 445–453 (2017).

[51] Chantre, C. O., Campbell, P. H., Golecki, H. M., Buganza, A. T., Capulli, A. K., Deravi, L. F. *et al.* Production-scale fibronectin nanofibers promote wound closure and tissue repair in a dermal mouse model. *Biomaterials* **166**, 96–108 (2018).

[52] Rawadi, G., Vayssière, B., Dunn, F., Baron, R., Roman-Roman, S. BMP-2 controls alkaline phosphatase expression and osteoblast mineralization by a Wnt autocrine loop. *J Bone Miner Res* **18**, 1842–1853 (2003).

[53] Yang, Y., Cheng, Y., Deng, F., Shen, L., Zhao, Z., Peng, S. *et al.* A bifunctional bone scaffold combines osteogenesis and antibacterial activity via *in situ* grown hydroxyapatite and silver nanoparticles. *Bio-Des Manuf* **4**, 452–468 (2021).

[54] Mansoorian, P., Ajorloo, M., Najmoddin, N. Engineered GO with magnetic iron oxide nanoparticles promotes osteogenic differentiation on 3D printed PCL scaffold. Diam Relat Mater 156, 112424 (2025).

[55] Kuttappan, S., Mathew, D., Nair, M. B. Biomimetic composite scaffolds containing bioceramics and collagen/gelatin for bone tissue engineering – a mini review. *Int J Biol Macromol* **93**, 1390–1401 (2016).

[56] Caddeo, S., Mattioli-Belmonte, M., Cassino, C., Barbani, N., Dicarlo, M., Gentile, P. *et al.* Newly designed collagen/polyurethane bioartificial blend as coating on bioactive glass–ceramics for bone tissue engineering applications. *Mater Sci Eng C* **96**, 218–233 (2019).

[57] Cho, Y. S., Kim, H.-K., Ghim, M.-S., Hong, M. W., Kim, Y. Y., Cho, Y.-S. Evaluation of the antibacterial activity and cell response for 3D-printed polycaprolactone/nanohydroxyapatite scaffold with zinc oxide coating. *Polymers* **12**, 2193 (2020).

[58] Ilyas, K., Akhtar, M. A., Ammar, E. B., Boccaccini, A. R. Surface modification of 3D-printed PCL/BG composite scaffolds via mussel-inspired polydopamine and effective antibacterial coatings for biomedical applications. *Materials* **15**, 8289 (2022).

[59] Lu, Z., Xiao, J., Wang, Y., Meng, M. *In situ* synthesis of silver nanoparticles uniformly distributed on polydopamine-coated silk fibers for antibacterial application. *J Colloid Interface Sci* **452**, 8–14 (2015).

[60] Song, Y., Jiang, H., Wang, B., Kong, Y., Chen, J. Silver-incorporated mussel-inspired polydopamine coatings on mesoporous silica as an efficient nanocatalyst and antimicrobial agent. *ACS Appl Mater Interfaces* **10**, 1792–1801 (2018).

Appendix

Table S1. RT-qPCR primer sequences, amplicon sizes, and validation metrics for mouse osteogenic marker genes

Gene mouse	RefSeq accession	Forward primer (5′→3′)	Reverse primer (5′→3′)	Amplicon size (bp)	Efficiency (%)	R^2	Product Tm (°C)
Runx2	NM_009820	ACTCTTCTGGAGCCGTTTATG	GTGAATCTGGCCATGTTTGTG	143	98	0.998	83.5
Bmp2	NM_007553	ACACAGCTGGTCACAGATAAG	CTTCCGCTGTTTGTGTTTGG	138	101	0.999	84.0
Ocn/Bglap	NM_001032298	AAGCAGGAGGGCAATAAGGT	TTTGTAGGCGGTCTTCAAGC	120	103	0.996	82.7
Gapdh	NM_008084	GGTGAAGGTCGGTGTGAACG	CCCGTAGGGCGATTACAGTC	143	99	0.997	83.2

Table S2. Summary of mechanical properties, normality, and homogeneity tests for PCL and PCL–Ag scaffolds (PBS, 37 °C). Values are expressed as mean ± SD (n = 6). Shapiro–Wilk p values confirm normal distributions for each metric; Levene's p values indicate equal variances between groups. Two-sample t tests show no significant difference in Young's modulus, UTS, or elongation at break ($p > 0.05$), demonstrating mechanical equivalence of the two scaffold types

Group	E_{mean}	E_{sd}	UTS_{mean}	UTS_{sd}	Eb_{mean}	Eb_{sd}	n	Shapiro $_{pE}$	Shapiro $_{pUTS}$	Shapiro $_{peb}$
PCL	20.028866950945595	2.1898586514911997	3.9786639076069537	0.4371485302611644	1.121976647206005	0.09500814910078081	6	0.061631566769345156	0.34204232831368975	0.415007187312346547
PCL-Ag	18.109984339865097	4.587867138983537	3.5808142502926175	0.3313175851501421	1.237489574645537 9	0.10701911487227264	6	0.309099092940803 07	0.3241520997213316	0.773205819703744

Table S3. EdU labeling index and imaging-based nuclei density for MC3T3-E1 on PCL vs PCL–Ag scaffolds at days 1, 3, 5, and 7 (mean ± SD; *n* = 4 independent scaffolds per group per time point)

Day	Group	EdU labeling index (%)	Nuclei density (cells·mm^{-2})
1	PCL	15.2 ± 3.0	850 ± 110
1	PCL–Ag	15.6 ± 3.2	870 ± 120
3	PCL	24.5 ± 4.0	1,250 ± 150
3	PCL–Ag	31.2 ± 3.8	1,510 ± 160
5	PCL	32.8 ± 4.5	1,720 ± 180
5	PCL–Ag	40.6 ± 4.1	2,080 ± 190
7	PCL	38.9 ± 5.2	2,100 ± 220
7	PCL–Ag	46.8 ± 4.9	2,550 ± 230

Table S4. Quantitative Live/Dead assay results showing the percentage of viable (Calcein$^+$) and dead (PI$^+$) cells on PCL–Ag and neat PCL scaffolds over 1–28 days of culture (mean values, n = 3 scaffolds, five fields per scaffold)

Day	PCL–Ag Viability (% Calcein$^+$)	PCL–Ag Dead (% PI$^+$)	PCL Viability (% Calcein$^+$)	PCL Dead (% PI$^+$)
1	97	3	91	9
3	96	4	90	10
7	95	5	90	10
14	94	6	89	11
21	94	6	89	11
28	93	7	89	11

Table S5. Quantitative morphometry of MC3T3-E1 cells on PCL (−Ag) vs PCL–Ag at 24 h

Metric (unit)	PCL (−Ag) mean ± SD	PCL–Ag mean ± SD	Δ% vs PCL	n (cells/objects)	p value	Effect size (Cohen's d)
Cell area (μm²)	1,250 ± 310	1,720± 360	+37.6%	465 / 472	<0.001	1.40
Aspect ratio (—)	1.62 ± 0.29	2.05± 0.33	+26.5%	465 / 472	<0.001	1.40
Circularity (0–1)	0.74 ± 0.08	0.61 ± 0.09	−17.6%	465 / 472	<0.001	1.55
Solidity (0–1)	0.87 ± 0.05	0.90 ± 0.04	+3.4%	465 / 472	0.002	0.65
Perimeter (μm)	160 ± 35	190 ± 40	+18.8%	465 / 472	<0.001	0.80
Nuclear area (μm²)	115 ± 20	125 ± 22	+8.7%	465 / 472	0.014	0.48
F-actin coherency (0–1)*	0.42 ± 0.08	0.55 ± 0.07	+31.0%	15 / 15 (fields)	<0.001	1.74

Table S6. Primer Sequences and PCR Efficiencies

Gene	Forward Primer (5′→3′)	Reverse Primer (5′→3′)	Amplicon Size (bp)	Efficiency (%)
RUNX2	CCA TCC TGC CTT CGT GCT T	CAG GTG GCT GGT AGT GAG A	132	98
BMP2	GGA GGA TGT TCA GGA TGC AA	GCT TCC GCT GTT TGT GTT TG	148	95
OCN	CTC TCT GCT CCG CTC TGT CT	TCA TGT GGT CAG CCA CAG TC	120	92
GAPDH	TGA AGG TCG GTG TGA ACG GAT TTG	CAT GTA GGC CAT GAG GTC CAC CAC	151	99

Table S7. RT-qPCR Raw Data and Relative Expression Analysis

Gene	Day	Sample (n=3)	Ct (Mean ± SD)	ΔCt (Ct_target –Ct_GAPDH)	ΔΔCt (vs. PCL control)	Fold Change (2^–ΔΔCt)
RUNX2	7	PCL	25.6 ± 0.3	7.2	0	1.00
		PCL–Ag	24.1 ± 0.2	5.8	–1.4	2.64
	14	PCL	25.4 ± 0.4	7.0	0	1.00
		PCL–Ag	23.9 ± 0.3	5.6	–1.4	2.64
BMP2	14	PCL	26.8 ± 0.5	8.4	0	1.00
		PCL–Ag	25.2 ± 0.3	6.7	–1.7	3.25
OCN	21	PCL	27.4 ± 0.4	9.0	0	1.00
		PCL–Ag	26.1 ± 0.2	7.7	–1.3	2.46

Table S8. Day-21 Alizarin Red S (ARS) mineralization on PCL vs PCL–Ag scaffolds in MC3T3-E1 cultures

Group	Biological replicate	ARS A405 / mg protein (mean of 3 tech reps)	Within-replicate SD	Within-replicate CV (%)
PCL	BR1	0.52	0.03	5.8
	BR2	0.61	0.02	3.3
	BR3	0.73	0.04	5.5
PCL (summary)		0.62	0.105	16.9
PCL–Ag	BR1	0.82	0.03	3.7
	BR2	0.93	0.02	2.2
	BR3	0.98	0.05	5.1
PCL–Ag (summary)		0.91	0.082	9.0

10.57647/jnsc.2026.1601.01

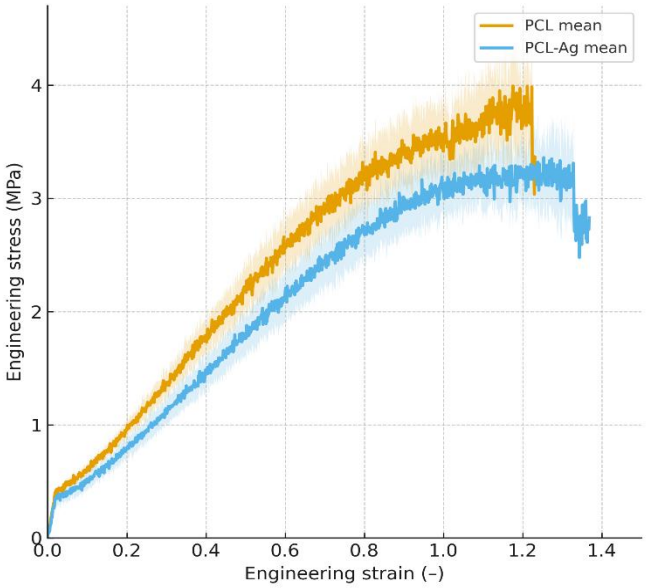

Figure S1. Representative mean engineering stress–strain curves (±95 % confidence interval) for neat PCL and Ag-decorated PCL scaffolds tested in PBS at 37 °C (n = 6 per group).

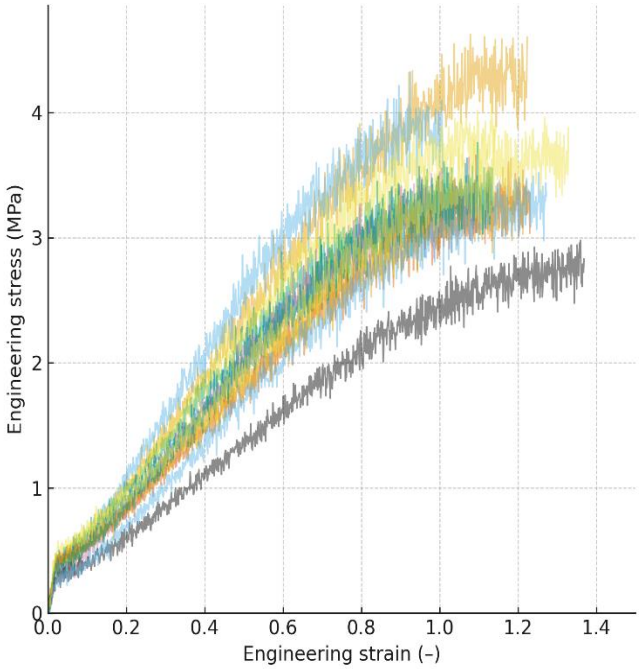

Figure S2. *Individual engineering stress–strain curves for all specimens (n = 6 per group)*

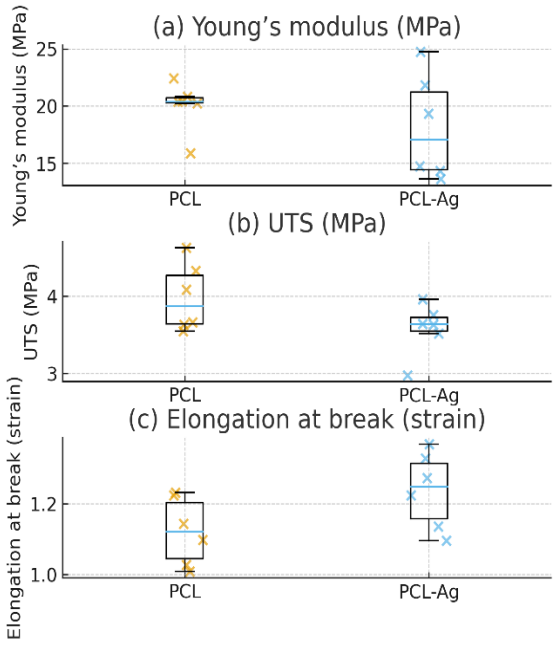

Figure S3. Statistical distributions of mechanical parameters for PCL and PCL–Ag scaffolds. (a) Young's modulus; (b) ultimate tensile strength (UTS); (c) elongation at break. Boxplots with overlaid points represent per-specimen values (mean ± SD)

10.57647/jnsc.2026.1601.01